Earth, Planets and Space

EXPRESS LETTER Open Access

High-latitude thermospheric wind study using a Fabry–Perot interferometer at Tromsø in Norway: averages and variations during quiet times

Heqiucen Xu[1*], Kazuo Shiokawa[1], Shin-ichiro Oyama[1,2,3] and Satonori Nozawa[1]

Abstract

The average winds in the thermosphere during geomagnetically quiet times are important because they provide a baseline wind in the upper atmosphere, but they remain insufficiently understood at high latitudes. This paper reports the first direct ground-based wind measurements of the quiet-time thermospheric wind pattern at Tromsø in Norway using 2009–2015 data from a Fabry–Perot interferometer. We analyzed red-line wind measurements (630.0 nm; altitude: 200–300 km). On average, the zonal wind shows a decrease of eastward wind compared with diurnal tidal wind before midnight. A maximum speed of 100 m/s occurs at both the dusk and dawn sides. The meridional wind has a diurnal tide structure with a minimum value of − 130 m/s around midnight. We also found occasional large wind deviations (> 100 m/s) from the averages, even during geomagnetically quiet times. We suggest that these large wind deviations are caused by the plasma convection associated with weak substorm activities with auroral electrojet (AE) index values of less than 100 nT that occurred at local times different from that at Tromsø.

Keywords: Fabry–Perot interferometer, Average wind, Thermosphere

Introduction

At high latitudes, the neutral wind in the thermosphere can be affected strongly by energy inputs from the magnetosphere during geomagnetically active times. Various important mechanisms can drive high-latitude winds, such as tides, plasma convections, and Joule heating. Both ground-based and in situ wind measurements are used widely to study how the neutral wind in the thermosphere responds to geomagnetic activities such as auroras and/or different substorm phases (e.g., Price and Jacka 1991; Price et al. 1995; Conde and Smith 1998; Conde et al. 2018; Kosch et al. 2010; Xu et al. 2019; Ritter et al. 2010; Oyama et al. 2016). Besides these studies focused on winds during disturbed times, others have investigated the high-latitude wind pattern and how it depends on various factors such as solar and geomagnetic conditions (e.g., Aruliah et al. 1991; Lathuillère et al. 1997).

The average winds during geomagnetically quiet times are important because they provide a baseline wind in the upper atmosphere. At high latitudes, the quiet-time wind pattern can be influenced by geomagnetic activity, although previous studies have used the Kp or Ap index to define the globally quiet condition. At the F-region height, previous studies have shown the quiet-time wind patterns at high latitudes (e.g., Witasse et al. 1998; Emmert et al. 2006a, b). Aruliah et al. (1999) investigated the Kp dependence of thermospheric winds at Kiruna in Sweden using a Fabry–Perot interferometer (FPI) via the 630 nm airglow/auroral emission. However, they used only the north and west scans of the FPI, measurements that were quite different from those made in the present study; the details are discussed in the section entitled "Comparison with F-region wind at Kiruna." Dhadly et al. (2017) focused on the seasonal dependence of the quiet-time winds in the northern high latitudes using

*Correspondence: xuheqiucen@isee.nagoya-u.ac.jp
[1] Institute for Space-Earth Environmental Research (ISEE), Nagoya University, Chikusa-ku, Nagoya 464-8601, Japan
Full list of author information is available at the end of the article

measurements from both FPIs and multiple satellites. However, the quiet-time thermospheric winds at Tromsø are yet to be investigated using ground-based FPI. The high-latitude thermospheric wind can be affected by localized geomagnetic activities such as particle precipitation and ion drag (e.g., Batten and Rees 1990; Oyama et al. 2009). Such a study at the European Incoherent Scatter (EISCAT) radar site at Tromsø is necessary and constructive for future studies of thermospheric dynamics, because the wind pattern during geomagnetically weak and quiet times provides a baseline for thermospheric dynamics without geomagnetic disturbances.

In the present study, we report the first direct measurements of the quiet-time average winds in the thermosphere at Tromsø in Norway using an FPI via the 630 nm emission. We also report a few events that exhibited large deviations (>100 m/s) from the average winds in the thermosphere even during geomagnetically quiet times, and we discuss their possible causes.

Instruments and data sets

The FPI used in this study is located in Tromsø, Norway, where the local time (LT) is 1 h ahead of universal time (UT) and the magnetic local time (MLT) is ~2.5 h ahead of UT. The FPI scans the sky in the five directions of north, west, south, east, and zenith as one set of vector wind measurements. In each direction, the 630.0 nm and 557.7 nm emissions are observed in sequence. The elevation angle of the sky scan is 45°, and the field of view (FOV) in each direction is 5° in full angle. The wind data have a time resolution of ~13 min. Detailed information about this FPI can be found in Shiokawa et al. (2012).

For the present average wind study, we checked all the wind data collected during 2009–2015 from the red-line emission (wavelength: 630.0 nm). The emission altitude of the 630 nm airglow is 200–300 km in the thermosphere, and therefore the FPI-derived winds are weighted values through the 630 nm emission profile. In the selected wind measurements that satisfied the quiet conditions, most of the data were obtained in the winter, as summarized in Table 1. For most dates, both zonal and meridional wind measurements were available.

The all-sky auroral images used in the present study were obtained by a collocated all-sky camera provided by the National Institute of Polar Research (NIPR) of Japan. This camera has an FOV of 180° with a fisheye lens. The magnetometer data were obtained from the International Monitor for Auroral Geomagnetic Effects (IMAGE) magnetometer network. We used the magnetograms obtained at the Tromsø and Bear Island (BJN) stations, which are located at almost the same geographic longitude of ~19°E. The Tromsø site is located at a geographic (geomagnetic) latitude of 69.58°N (66.73°N), while the BJN site is located at 74.50°N (71.45°N).

Table 1 List of wind data used in this study

Year	Dates with measurements
2009	1.23–1.25, 1.28, 1.29, 2.17, 2.18, 11.10, 11.11, 11.13, 11.14, 11.17–11.20, 11.24, 11.27, 12.6–12.8, 12.25
2010	2.18, 3.2
2011	2.23, 2.24, 11.19
2012	9.28, 11.23, 12.23
2013	–
2014	1.19, 11.13
2015	–

Method

We applied strict criteria to define geomagnetically quiet times. We began by choosing the interval of FPI operation under clear-sky conditions (status "s" and "p"), identified using the hourly status from a collocated all-sky airglow imager of the Optical Mesosphere Thermosphere Imagers (OMTIs, http://stdb2.isee.nagoya-u.ac.jp/omti/) (Shiokawa et al. 2009). Then, for step 1, we used $Kp \leq 1^+$ to ensure globally quiet conditions both at the time of the wind measurement and 3–6 h before the wind measurement because neutral gas can take that long to recover after being influenced by geomagnetic activity at high latitude (Aruliah et al. 1999).

For step 2, we ensured locally quiet conditions at Tromsø. We defined baseline X-component values at Tromsø at each time sector for each year, as shown in Table 2. Each baseline value was chosen from the first clear quiet day of that year as determined by visual inspection, presented as 1-h averages. If no value was available for a given year, then we used the corresponding value from the previous year. We defined a non-quiet interval as being when the absolute difference between the X-component value and the baseline exceeded 50 nT. An isolated substorm event was defined as a continuous series of non-quiet intervals that lasted for more than 1 h, and the first (last) non-quiet interval was defined as the start (end) of the isolated substorm event. As shown in Fig. 1, we excluded any wind measurements made either during or up to 3 h after these substorm events.

For step 3, we checked the all-sky images at Tromsø and excluded any measurements made when auroral activities were penetrating the FPI scanning region. Quiet-time periods were defined as those that satisfied the criteria in steps 1–3. After further excluding some measurements with suspicious cloud influences as identified by the all-sky auroral camera, the qualifying

Table 2 Baseline values of X component of magnetometer data at Tromsø

Year	Dusk (14-20 UT)	Midnight (20-2 UT)	Dawn (2-8 UT)	Date of the chosen value
2009	10,910.4	10,901.2	10,886.4	26 Jan 2009
2010	10,903.2	10,902.6	10,903.0	8 Feb 2010
2011	10,893.9	10,888.7	10,890.9	27 Jan 2011
2012	10,893.9[a]	10,888.7[a]	10,890.9[a]	–
2013	10,847.3	10,846.4	10,850.1	4 Oct 2013
2014	10,852.4	10,849.9	10,850.1[a]	13 Feb 2014
2015	10,852.4[a]	10,849.9[a]	10,850.1[a]	–

Unit: nT

[a] We used the same corresponding value in the previous year

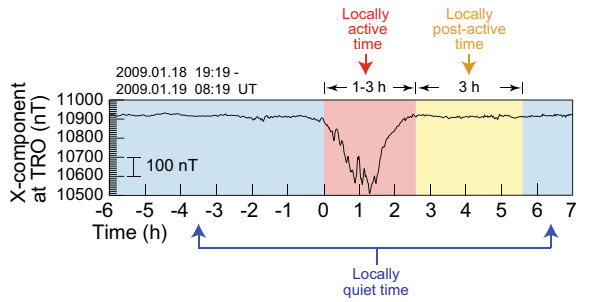

Fig. 1 Definition of locally quiet time at Tromsø

quiet-time measurements were used to calculate the average winds.

Finally, for step 4, we used these qualifying measurements to calculate the initial 30-min-average winds (the thick gray curves in Fig. 2c, d) from the red-line (630 nm) emission. Despite being selected as measurements made during geomagnetically quiet times, some exceptional wind measurements exhibited large deviations from the initial average winds, as marked by the red asterisks in Fig. 2c, d. The deviations were more than 100 m/s from the initial averages, which may have been caused by geomagnetic activities not identified in steps 1–4. We therefore removed these exceptional wind measurements with large deviations of more than 100 m/s from the initial averages in the qualifying measurements. The remaining data were used to recalculate the final quiet-time average winds as shown by the blue and green curves in Fig. 2a, b, respectively. The same blue and green curves are present in Fig. 2c, d, respectively, but they mostly overlap with the initial averages shown as the gray curves. We discuss the possible causes of the aforementioned exceptional measurements in "Events with large deviations from averages, and related discussion".

Quiet-time average winds

Figure 2a, b shows the quiet-time average winds in the thermosphere in the zonal and meridional directions, respectively. The half-length of an error bar corresponds to the standard deviation of all the winds used to calculate the average in that bin. As shown in Fig. 2c, d, there were 5–20 wind measurements in each 30-min bin to calculate the average winds. We also plotted in yellow the quiet-time average winds at Kiruna in Sweden (67.87°N, 20.43°E in geographic coordinates) as obtained from Aruliah et al. (1999) and in red the average winds at Tromsø as obtained from the Horizontal Wind Model (HWM) (Drob et al. 2015).

Considering the diurnal tide, the zonal wind in Fig. 2a should be eastward before 2–3 UT and westward after 2–3 UT (e.g., Kohl and King 1967). However, we found that the zonal wind exhibits a decrease of eastward wind before midnight, with a minimum at 21–22 UT. After 22 UT, the wind recovers eastward and then decreases again after midnight. The zero crossing of the zonal wind after midnight occurs at ~3 UT. The maximum speed is ~100 m/s at both the dusk and dawn sides. The meridional wind in Fig. 2b shows an equatorward wind with a minimum value (−130 m/s) around midnight, which is a typical signature of a diurnal tide in the thermosphere.

Discussion of quiet-time average winds

Comparison with model and satellite winds

For the HWM14-derived winds in Fig. 2, we first calculated the model-based local winds corresponding to all the time segments used for our quiet-time average winds. We chose the simultaneous Ap index as the input of HWM14 and then calculated the averages in the same way as for the actual observations. Again, the half-length of an error bar corresponds to the standard deviation of all the winds used to calculate the average in that bin. In

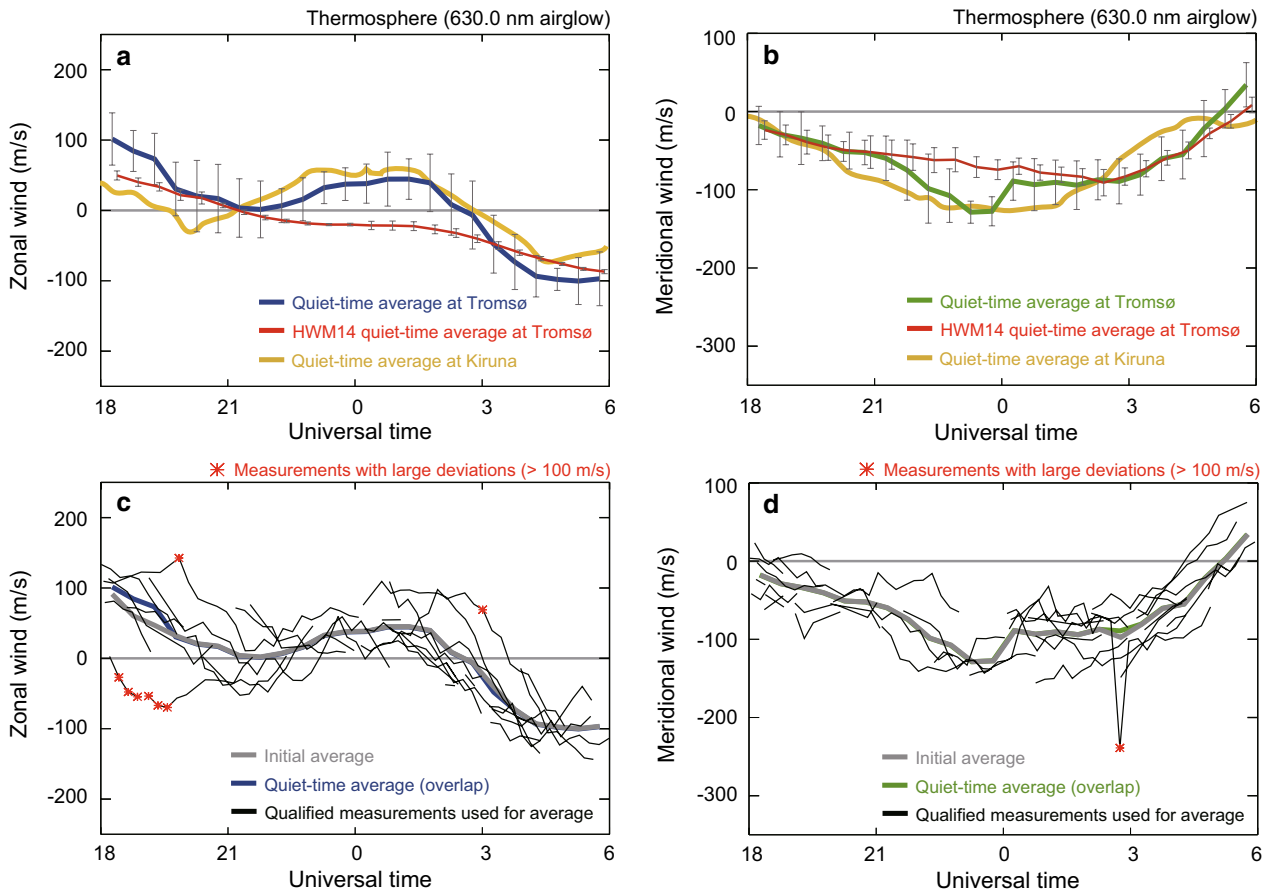

Fig. 2 Nightside quiet-time average wind in thermosphere (200–300 km) at Tromsø. The data were averaged in 0.5 h bins. **a**, **b** Quiet-time average zonal and meridional winds. In quiet times, the HWM14-derived average wind at Tromsø and average wind at Kiruna of Aruliah et al. (1999) are also shown. **c**, **d** Qualifying measurements satisfying both globally and locally quiet conditions, from which initial average wind (gray) is calculated. Red asterisks indicate those measurements with large deviations (> 100 m/s) from initial average winds, which were removed in calculating the final quiet-time averages. Note that we artificially shifted the HWM wind to a few minutes later to avoid overlapping error bars, although they were calculated using the same time bins as those for the quiet-time averages

the model, the thermosphere height was 250 km. Note that the HWM winds have been shifted artificially to a few minutes later in Fig. 2 to avoid overlapping error bars, although they were calculated using the same time bins as those used for the quiet-time average winds.

In Fig. 2b, the diurnal tide structure of the HWM14 meridional wind is consistent with actual observations, although the model predicts lower speeds near midnight. In Fig. 2a, HWM14 fails to predict the observed decrease of eastward wind before midnight. These results suggest that some improvements are required for the HWM to demonstrate the quiet-time winds at high latitudes.

The Gravity Field and Steady-State Ocean Circulation Explorer (GOCE) satellite provides direct wind measurements at both dawn and dusk sectors at an altitude of ~250 km. As shown in Fig. 8 of Dhadly et al. (2017), the quiet-time average cross-track wind in December Solstice at 65–70°N geomagnetic latitudes has a MLT coverage at ~6:30–9:00 and ~16:00–18:30, which correspond to ~4:00–6:30 UT and ~13:30–16:00 UT, respectively, at Tromsø. The average cross-track wind of GOCE at ~6:30 MLT is westward in geomagnetic coordinates with an amplitude of ~100 m/s, which is similar to the zonal wind at 4:00 UT in the present study in geographic coordinates.

Comparison with F-region wind at Kiruna

In Fig. 2a, b, we also show as the yellow curves the quiet-time average winds with $Kp \leq 2^-$ obtained from a 630 nm FPI at Kiruna in Sweden as obtained from Figure 1 of Aruliah et al. (1999). They averaged 42 ± 15 wind measurements in each 15-min bin. For the zonal

wind, both Tromsø and Kiruna exhibit an obvious decrease of eastward wind before midnight, something that Aruliah et al. (1999) suggested could be caused by westward plasma convection. At the F-region height, even though the effect from tidal components other than the diurnal tide is minor, the ion drag effect is more effective than at E-region height (e.g., Mayr and Harris 1978; Richmond et al. 2003). Therefore, we speculate that this decrease of eastward wind at Tromsø is most likely related to the westward plasma convection at the dusk side as well, which is expected from the usual two-cell convection pattern (e.g., Heppner and Maynard 1987; Thomas and Shepherd 2018).

Note that this decrease of eastward wind is slightly larger and earlier (before 20 UT) at Kiruna. This westward increase ceases and starts to increase eastward at ~20 UT at Kiruna and at ~22 UT at Tromsø. We therefore explore the possible reasons for this 2 h time difference. Aruliah et al. (1999) used north and west FPI scans at an elevation angle of 30°. If we assume that the thermospheric wind measurements in the present paper were obtained right above Tromsø at an altitude of 250 km, then the spatial differences in wind measurements between the present paper and Aruliah et al. (1999) are ~400 km and ~250 km for the zonal and meridional directions, respectively. At the zonal wind measurement point at Kiruna, the MLT is ~2.3 h ahead of UT and the geomagnetic latitude is ~65.20°N, both of which are close to the corresponding values at Tromsø (2.5 h, 66.64°N). Consequently, the timing difference of the westward increase and subsequent eastward increase in the zonal wind in Fig. 2a are unlikely to have been caused by the location difference.

Before midnight, the convection direction of ionospheric plasma changes abruptly from westward into eastward near the Harang discontinuity at the equatorward side of the auroral zone (e.g., Heppner and Maynard 1987; Erickson et al. 1991; Koskinen and Pulkkinen 1995), and the Harang discontinuity may be the cause of the decrease and subsequent increase of eastward wind in Fig. 2a. Aruliah et al. (1999) showed that the eastward turning of convection at the Harang discontinuity occurs at earlier MLT with increasing geomagnetic activities. In Fig. 2a, the zonal wind of Aruliah et al. (1999) was obtained with $Kp \leq 2^{-}$, whereas our result at Tromsø was obtained with $Kp \leq 1^{+}$. This difference in geomagnetic activity may be the cause of the timing difference of the decrease of eastward wind in Fig. 2a between Aruliah et al. (1999) and the present study. At dawn side, the different threshold of Kp index may also contribute to the different zonal winds between two stations.

Events with large deviations from averages and related discussion

In the thermosphere, we found five nights during which there were large deviations (>100 m/s) from quiet-time averages, as shown in Fig. 2c, d. For two of them (events with large deviations in zonal winds before 20 UT), we show the entire measurement over the corresponding night in Fig. 3a, b (event R1) and Fig. 3f, g (event R2).

In Fig. 3a, b, f, g, the blue rectangle at the top of the panel indicates the quiet-time period as defined in "Method" the red rectangle indicates the interval in which there is large deviation from the average winds, and the light blue curve indicates the quiet-time average winds shown in Fig. 2a, b. Figure 3c–e, h–j shows the X component of the magnetometer data, the auroral electrojet (AE) and amplitude lower (AL) indices, and the By and Bz components of the interplanetary magnetic field (IMF) in geocentric solar magnetospheric (GSM) coordinates. For events R1 and R2, the large deviations in zonal winds lasted for 0.5–1 h, while the meridional winds showed good consistency with the averages. Note the presence of substorm activity right after the event time in Fig. 3a, b; the aurora identified by the all-sky images expanded southward into the FPI scanning region at the same time. It was cloudy before 19 UT and after 22 UT as shown by the gray rectangles in Fig. 3f, g, and measurements made during these time periods were excluded when calculating the quiet-time average winds.

Before and during events R1 and R2, weak auroral activities were identified at the northern edge of the all-sky images at Tromsø. However, from the magnetometer data no substorm could be identified at BJN. Because the measurements and the average in the meridional direction are consistent, it is unlikely that the Joule heating on the thermosphere in the north of Tromsø caused these large zonal wind deviations. The AE and AL indices show some substorm activities with amplitudes of less than ~100 nT on a global scale, although we have $Kp \leq 1^{+}$ for both events. These substorms probably occurred elsewhere at different local times from that at Tromsø.

At high latitudes, the ion drag in the F-region is more effective than that in the E region (e.g., Mayr and Harris 1978; Richmond et al. 2003). Considering the general plasma convection pattern (e.g., Weimer 1995), westward convection is expected above Tromsø associated with these AE and AL activities before and during events R1 and R2. Therefore, we suggest that the plasma convection associated with substorms that occurred at different local times caused a westward drive to the thermosphere above Tromsø in these two events, although the ion motion may have been dominated by neutral wind at high latitudes under the

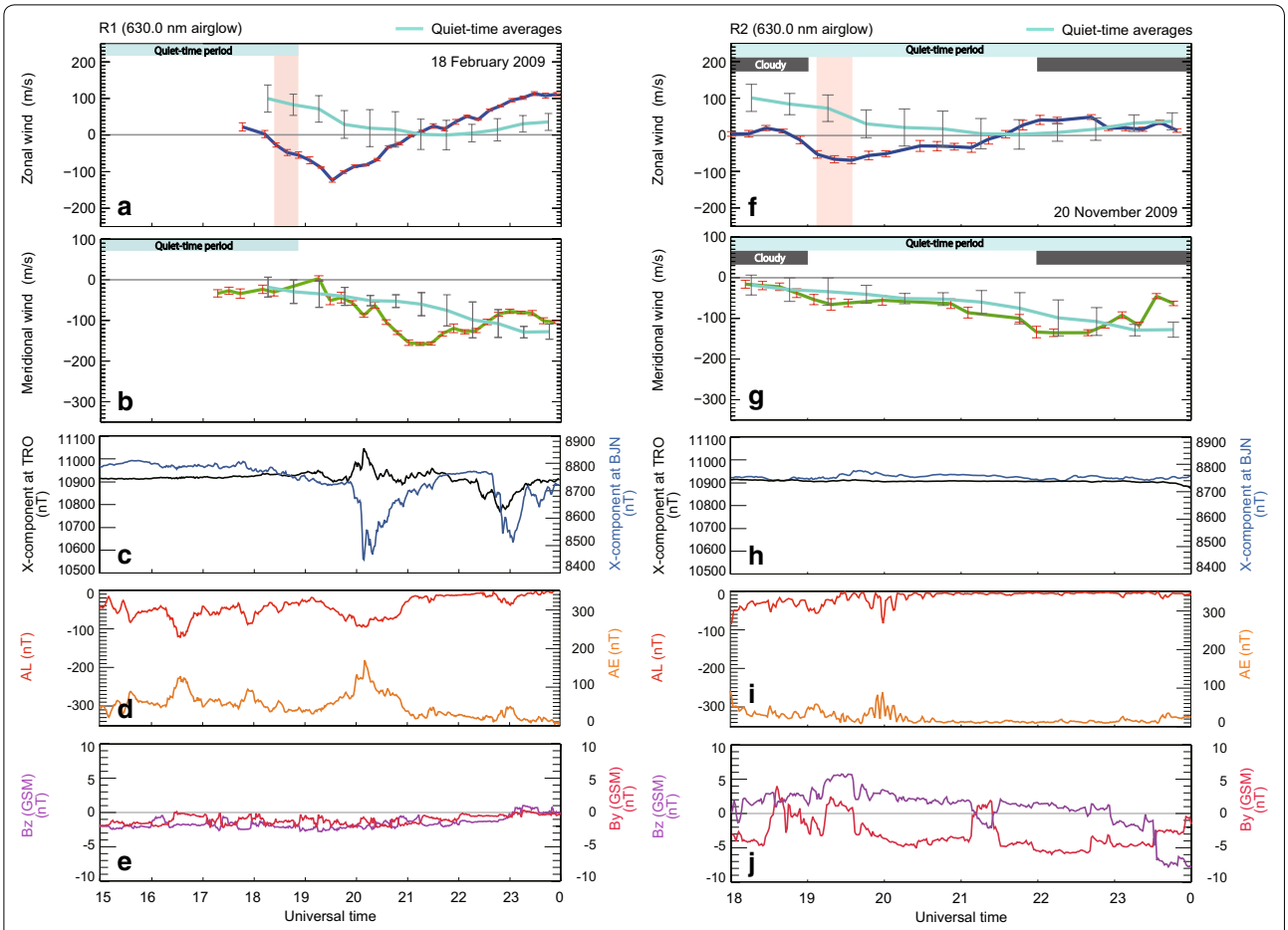

Fig. 3 Two thermospheric wind measurements (events R1 and R2) during quiet times, whose zonal wind showed large deviation (> 100 m/s) from quiet-time average. **a**, **f** Zonal wind. **b**, **g** Meridional wind. **c**, **h** X component of magnetometer data at Tromsø and Bear Island. **d**, **i** AE and AL indices. **e**, **j** IMF By and Bz in GSM coordinates. The blue rectangle indicates the quiet-time period, namely Kp $\leq 1^+$ for 3–6 h before, with no substorm or auroral activity being identified above Tromsø. The red rectangle indicates the interval of the deviated measurements. The light blue curve indicates the quiet-time average wind, and the dark-gray rectangles indicate times of cloud

condition of weak electric field (e.g., Fujii et al. 1998). Thus, even if small substorm activity with AE < 100 nT occurs at different local times, the zonal wind can deviate by more than 100 m/s at Tromsø.

We also checked the plasma data from the Super Dual Auroral Radar Network (SuperDARN) and EISCAT radar, as well as the global convection map from the SuperDARN radar and a data assimilation model (Ruohoniemi and Baker 1998). However, we could find no useful convection data for events R1 and R2. The convection pattern provided by the SuperDARN convection model showed a very small convection area at high latitudes (> 70°N in geomagnetic latitude), and Tromsø was outside that area. However, there may have been some westward convection at Tromsø that was too weak to be seen in the SuperDARN convection model.

Conclusions

Using an FPI at Tromsø in Norway, we focused on the high-latitude nightside thermospheric winds during geomagnetically quiet times. The wind data were collected from red-line emission (630.0 nm, altitude: 200–300 km) during 2009–2015. This is the first time that direct wind measurements from an FPI have been used to obtain the quiet-time average winds in the thermosphere at Tromsø. We also reported two events that exhibited large deviations (> 100 m/s) from the quiet-time average winds in the thermosphere. The main results of this paper are summarized as follows.

1. The average zonal wind at Tromsø exhibits a decrease of eastward wind from the diurnal tide before midnight, with a minimum value centered at 21–22 UT. This can be related to the westward plasma convection at the dusk side. After 22 UT, the zonal wind recovers eastward and then turns westward after midnight. The maximum speed of the zonal wind is ~100 m/s at both the dusk and dawn sides. The average meridional wind is an equatorward wind with a minimum value (−130 m/s) around midnight, which is a typical signature of a diurnal tide in the thermosphere. The wind pattern observed at Tromsø is generally similar to that at Kiruna as found previously by Aruliah et al. (1999), although the decrease of eastward wind at Tromsø before midnight occurs 2 h later than that at Kiruna.
2. At Tromsø, HWM14 predicts a meridional wind with smaller amplitude and fails to predict the eastward wind decrease in the zonal wind before midnight. This suggests that some improvements are necessary for the HWM to demonstrate the quiet-time winds at high latitudes.
3. For events with large deviations from the quiet-time average winds at Tromsø, we speculate that the westward increases of zonal wind (>100 m/s) in the thermosphere before midnight are caused by the plasma convection associated with weak substorm activities that occur at local times different from that at Tromsø. This fact indicates that even if small substorm activity with AE < ~100 nT occurs at different local times, the zonal wind can deviate by more than 100 m/s at Tromsø.

Abbreviations

BJN: Bear Island; EISCAT: European Incoherent Scatter; GSM: geocentric solar magnetospheric; HWM: Horizontal Wind Model; IMAGE: International Monitor for Auroral Geomagnetic Effects; IMF: interplanetary magnetic field; FPI: Fabry–Pérot interferometer; FOV: field of view; LT: local time; MLT: magnetic local time; NIPR: National Institute of Polar Research; UT: universal time.

Acknowledgements

The authors acknowledge the use of SuperDARN data. SuperDARN is a collection of radars funded by national scientific funding agencies of Australia, Canada, China, France, Italy, Japan, Norway, South Africa, UK, and the USA. We are indebted to the director and staff of EISCAT for operating the facility and supplying the data. EISCAT is an international association supported by research organizations in China (CRIPR), Finland (SA), Norway (NFR), Sweden (VR), and the UK (UKRI). We are indebted to Drs. H. Miyaoka and Y. Ogawa for operating the NIPR all-sky camera at Tromsø and supplying the data (http://polaris.nipr.ac.jp/~acaurora/aurora/Tromso/). We thank the institutes who maintain the IMAGE Magnetometer Array (http://space.fmi.fi/image/www/). We thank Prof. Mike Kosch who is the owner of the hut where the FPI was operated.

Authors' contributions

HX conducted the analysis and wrote the paper. KS guided this study as the graduate-course supervisor of HX. SO and SN helped with the FPI measurements and use of EISCAT data. All the authors read and approved the final manuscript.

Funding

This work was supported by JSPS KAKENHI (15H05815 and 16H06286). We are grateful for the support of the Leadership Development Program for Space Exploration and Research at Nagoya University.

Availability of data and materials

The FPI wind and temperature data used in this paper are available at ISEE, Nagoya University (http://stdb2.isee.nagoya-u.ac.jp/omti/). The AE, AL, Kp, and Ap indices were provided by the WDC for Geomagnetism at Kyoto University (http://wdc.kugi.kyoto-u.ac.jp). The authors acknowledge the use of the online tool hosted by the Virginia Tech SuperDARN group at their website (http://vt.superdarn.org/tiki-index.php). The IMF data were obtained from the GSFC/SPDF OMNIWeb interface (http://omniweb.gsfc.nasa.gov). The HWM14 model is available online (https://agupubs.onlinelibrary.wiley.com/doi/full/10.1002/2014EA000089). The MLT was calculated using the online tool at https://omniweb.gsfc.nasa.gov/vitmo/cgm.html.

Ethics approval and consent to participate

Not applicable.

Consent for publication

Not applicable.

Competing interests

The authors declare that they have no competing interests.

Author details

[1] Institute for Space-Earth Environmental Research (ISEE), Nagoya University, Chikusa-ku, Nagoya 464-8601, Japan. [2] Space and Upper Atmospheric Sciences Group, National Institute of Polar Research, 10-3, Midori-cho, Tachikawa-shi, Tokyo 190-8518, Japan. [3] University of Oulu, Pentti Kaiteran katu 1, Linnanmaa, 90540 Oulu, Finland.

Received: 23 July 2019 Accepted: 16 October 2019
Published online: 25 October 2019

References

Aruliah AL, Rees D, Fuller-Rowell TJ (1991) The combined effect of solar and geomagnetic activity on high latitude thermospheric neutral winds. Part I. Observations. J Atmos Terr Phys 53(6–7):467–483. https://doi.org/10.1016/0021-9169(91)90075-i

Aruliah AL, Müller-Wodarg ICF, Schoendorf J (1999) Consequences of geomagnetic history on the high-latitude thermosphere and ionosphere: averages. J Geophys Res 104(A12):28073–28088. https://doi.org/10.1029/1999JA900334

Batten S, Rees D (1990) Thermospheric winds in the auroral oval: observations of small scale structures and rapid fluctuations by a Doppler Imaging System. Planet Space Sci 38(5):675–694

Conde M, Smith RW (1998) Spatial structure in the thermospheric horizontal wind above Poker Flat, Alaska, during solar minimum. J Geophys Res 103(A5):9449–9471. https://doi.org/10.1029/97JA03331

Conde M, Bristow WA, Hampton DL, Elliott J (2018) Multiinstrument studies of thermospheric weather above Alaska. J Geophys Res 123:9836–9861. https://doi.org/10.1029/2018JA025806

Dhadly M, Emmert J, Drob D, Conde M, Doornbos E, Shepherd G, Makela J, Wu Q, Niciejewski R, Ridley A (2017) Seasonal dependence of northern high-latitude upper thermospheric winds: a quiet time climatological study based on ground-based and space-based measurements. J Geophys Res 122:2619–2644. https://doi.org/10.1002/2016JA023688

Drob DP, Emmert JT, Meriwether JW, Makela JJ, Doornbos E, Conde M, Hernandez G, Noto J, Zawdie KA, McDonald SE et al (2015) An update to the Horizontal Wind Model (HWM): the quiet time thermosphere. Earth Space Sci 2:301–319. https://doi.org/10.1002/2014EA000089

Emmert JT, Faivre ML, Hernandez G, Jarvis MJ, Meriwether JW, Niciejewski RJ, Sipler DP, Tepley CA (2006a) Climatologies of nighttime upper thermospheric winds measured by ground-based Fabry-Perot interferometers during geomagnetically quiet conditions: 1. Local time, latitudinal, seasonal, and solar cycle dependence. J Geophys Res 111:A12302. https://doi.org/10.1029/2006ja011948

Emmert JT, Hernandez G, Jarvis MJ, Niciejewski RJ, Sipler DP, Vennerstrom S (2006b) Climatologies of nighttime upper thermospheric winds measured by ground-based Fabry-Perot Interferometers during geomagnetically quiet conditions: 2. High-latitude circulation and IMF dependence. J Geophys Res 111:A12303. https://doi.org/10.1029/2006ja011949

Erickson GM, Spiro RW, Wolf RA (1991) The physics of the Harang discontinuity. J Geophys Res 96(A2):1633–1645. https://doi.org/10.1029/90JA02344

Fujii R, Nozawa S, Buchert SC, Matuura N, Brekke A (1998) The motion of ions in the auroral ionosphere. J Geophys Res 103(A9):20685–20695. https://doi.org/10.1029/98JA01685

Heppner JP, Maynard NC (1987) Empirical high-latitude electric field models. J Geophys Res 92(A5):4467–4489. https://doi.org/10.1029/JA092iA05p04467

Kohl H, King JW (1967) Atmospheric winds between 100 and 700 km and their effects on the ionosphere. J Atmos Terr Phys 29:1045–1062. https://doi.org/10.1016/0021-9169(67)90139-0

Kosch MJ, Anderson C, Makarevich RA, Carter BA, Fiori RAD, Conde M, Dyson PL, Davies T (2010) First E region observations of mesoscale neutral wind interaction with auroral arcs. J Geophys Res 115:A02303. https://doi.org/10.1029/2009JA014697

Koskinen HEJ, Pulkkinen TI (1995) Midnight velocity shear zone and the concept of Harang discontinuity. J Geophys Res 100(A6):9539–9547. https://doi.org/10.1029/95JA00228

Lathuillère C, Lilensten J, Gault W, Thuillier G (1997) Meridional wind in the auroral thermosphere: results from EISCAT and WINDII-O(1 D) coordinated measurements. J Geophys Res 102(A3):4487–4492. https://doi.org/10.1029/96JA03429

Mayr HG, Harris I (1978) Some characteristics of electric field momentum coupling with the neutral atmosphere. J Geophys Res 83(A7):3327–3336. https://doi.org/10.1029/JA083iA07p03327

Oyama S, Tsuda TT, Sakanoi T, Obuchi Y, Asamura K, Hirahara M, Yamazaki A, Kasaba Y, Fujii R, Nozawa S, Watkins BJ (2009) Spatial evolution of frictional heating and the predicted thermospheric wind effects in the vicinity of an auroral arc measured with the Sondrestrom incoherent-scatter radar and the Reimei satellite. J Geophys Res Space Phys. https://doi.org/10.1029/2009JA014091

Oyama S, Shiokawa K, Miyoshi Y, Hosokawa K, Watkins BJ, Kurihara J, Tsuda TT, Fallen CT (2016) Lower thermospheric wind variations in auroral patches during the substorm recovery phase. J Geophys Res 121:3564–3577. https://doi.org/10.1002/2015JA022129

Price GD, Jacka F (1991) The influence of geomagnetic activity on the upper mesosphere/lower thermosphere in the auroral zone. I. Vertical winds. J Atmos Terr Phys 53:909–922. https://doi.org/10.1016/0021-9169(91)90004-Q

Price GD, Smith RW, Hernandez G (1995) Simultaneous measurements of large vertical winds in the upper and lower thermosphere. J Atmos Terr Phys 57:631–643. https://doi.org/10.1016/0021-9169(94)00103-U

Richmond AD, Lathuillère C, Vennerstroem S (2003) Winds in the high-latitude lower thermosphere: dependence on the interplanetary magnetic field. J Geophys Res 108(A2):1066. https://doi.org/10.1029/2002JA009493

Ritter P, Lühr H, Doornbos E (2010) Substorm-related thermospheric density and wind disturbances derived from CHAMP observations. Ann Geophys 28:1207–1220. https://doi.org/10.5194/angeo-28-1207-2010

Ruohoniemi JM, Baker KB (1998) Large-scale imaging of high-latitude convection with Super Dual Auroral Radar Network HF radar observations. J Geophys Res 103(A9):20797–20811. https://doi.org/10.1029/98JA01288

Shiokawa K, Hosokawa K, Sakaguchi K, Ieda A, Otsuka Y, Ogawa T, Connors M (2009) The Optical Mesosphere Thermosphere Imagers (OMTIs) for network measurements of aurora and airglow, future perspectives of space plasma and particle instrumentation and international collaborations. In: Hirahara M, Miyoshi Y, Terada N, Shinohara I, Mukai T, editors. AIP Conference proceedings, AIP Conference proceedings, pp 212–215. https://doi.org/10.1063/1.3169292

Shiokawa K, Otsuka Y, Oyama S, Nozawa S, Satoh M, Katoh Y, Hamaguchi Y, Yamamoto Y, Meriwether J (2012) Development of low-cost sky-scanning Fabry-Perot interferometers for airglow and auroral studies. Earth Planets Space 64(11):1033–1046. https://doi.org/10.5047/eps.2012.05.004

Thomas EG, Shepherd SG (2018) Statistical patterns of ionospheric convection derived from mid-latitude, high-latitude, and polar SuperDARN HF radar observations. J Geophys Res 123:3196–3216. https://doi.org/10.1002/2018JA025280

Weimer DR (1995) Models of high-latitude electric potentials derived with a least error fit of spherical harmonic coefficients. J Geophys Res 100:19595–19607. https://doi.org/10.1029/95JA01755

Witasse O, Lilensten J, Lathuillère C et al (1998) Meridional thermospheric neutral wind at high latitude over a full solar cycle. Ann Geophys 16:1400. https://doi.org/10.1007/s00585-998-1400-3

Xu H, Shiokawa K, Oyama S-i, Otsuka Y (2019) Thermospheric wind variations observed by a Fabry-Perot interferometer at Tromsø, Norway, at substorm onsets. Earth Planets Space 71:93

Publisher's Note